 FDMP, vol.7, no.1, pp.29-56, 2011

A Numerical Simulation Study of Silicon Dissolution under Magnetic Field

A. Kidess[1], N. Armour[1] and S. Dost[1,2]

Abstract: When a metallic liquid is subject to strong magnetic body forces, the issues of convergence and numerical stability may arise in numerical simulations. Handling of magnetic body force terms needs care. In this work we have studied two open codes and discussed the related issues. Magnetic force and mass transport terms were added to these codes. Handling the stability issues was discussed. The developed systems were validated by two benchmark cases.
Then, the dissolution process of silicon into the germanium melt was selected as an application. The objective was the numerical study of the dissolution process with and without the application of an applied static magnetic field to examine the conditions used in experiments. The simulation results agree with experiments in both cases in predicting concentration distribution in the melt. However, they do not predict the experimentally observed enhanced dissolution structure near the ampoule wall along the source/melt interface under magnetic field.

Keywords: numerical simulation, dissolution, magnetic fields, convection.

1 Introduction

The use of computational packages that do not make the source code available to the user may present challenges in handling strong magnetic body forces in numerical simulations. It may even lead to erroneous results due to the treatment of the source terms (Kumar, Dost and Durst(2007)). As discussed later in detail, the main reason for this is that such forces are coupled with the flow velocity components and also have large differences in magnitude with respect to the gravitational body force term. The issue, of course, may become easier if the source code is available. In this work we utilize two of such open codes.

Numerous numerical simulation codes are available under an open source license and vary widely in their capabilities, documentation, and community involvement.

[1] Crystal Growth Laboratory, University of Victoria, Victoria, BC Canada V8W 3P6
[2] Corresponding Author: sdost@me.uvic.ca; Tel: +1 250 721 8898, Fax: +1 250 721 6294.

NOMENCLATURE

$\mathbf{B}$	applied magnetic field in Tesla
N	buoyancy ratio
D	diffusion coefficient of silicon species in germanium melt
σ	electric conductivity of the liquid phase
$\mathbf{u}$	flow velocity vector
	flow velocity cartesian components
∇ , ∇	gradient and Laplacien operators in cylindrical coordinates, respectively.
g	gravitational constant
Gr	Grashof number
Ha	Hartmann number
$\mathbf{F}$	magnetic body force
μ_M	magnetic permeability
ρ	mass density of the liquid phase
Pa	Prandtl number
P	pressure
Ra	Rayleigh number
p	total pressure
C	silicon molar fraction
C_0	silicon initial molar fraction
	specific heat of the liquid phase
β	solutal expansion coefficient
T	temperature
λ	thermal conductivity of the liquid phase
β	thermal expansion coefficient
t	time
$\mathbf{n}$	unit normal vector
μ	viscosity of the liquid phase

Although these codes are mostly used by the academic institutions where originated, some of them have gained sufficient momentum to sustain a contributing user community. Two codes that satisfy the requirements for the intention of this work are OpenFOAM (FOAM = field operation and manipulation) and FASTEST 3D (Flow Analysis by Solving Transport Equations Simulating Turbulence 3-Dimensional).

FASTEST has been extensively used for simulations of fluid flow and crystal growth at the Fluid Mechanics Institute of the University of Erlangen-Nuremberg. It is a finite volume based CFD code working with multiblock structured meshes and is available under an open source academic license.

OpenFOAM is a general framework to solve partial differential equations developed at the London Imperial College, with most of the standard solvers targeting fluid dynamics problems. OpenFOAM is written in C++ and makes good use of object-oriented design principles, which enables the development of elegant "applications" that directly resemble the underlying partial differential equations. It is very flexible due to a wide selection of linear solvers and interpolation techniques, and boasts a large user community and available commercial consulting.

We first used FASTEST to simulate the dissolution process due to its maturity with respect to crystal growth problems (see for instance Kumar, Dost and Durst(2007); and Jana, Dost, Kumar and Durst(2006)). However, throughout the work, some problems associated with the magnetic field implementation became apparent that could not be resolved. An OpenFOAM solver was then developed and utilized. Simulation results are first compared with the flow structures obtained with FASTEST and Ansys CFX in the absence of magnetic body forces. Once confidence was gained on the code, simulations were carried out under magnetic field.

The objective of the present study was to simulate the dissolution process of silicon into the germanium melt due to its significance in crystal growth of SiGe.

1.1 Silicon Germanium (SiGe) Single Crystals

There has been recent interest in the silicon germanium alloy (Si_xGe_{1-x}) as an emerging semiconductor material since it possesses full miscibility across its composition range allowing for adjustment of the band gap and lattice parameter (Kasper (1995); Seidenberg (1997)). Bulk single crystals of Si_xGe_{1-x} have application in photodetection, photovoltaics, thermal imaging, and as a substrate for Si_xGe_{1-x} epitaxial layers (Usami, Kitamura, Obara, Nose, Shishido, and Nakajima (2005)). The bulk Si_xGe_{1-x} substrates can be lattice-matched to the device layer, reducing strain. Among device structures of interest, the heterobipolar transistor has been most studied due to its applications in telecommunications. As for other important applications for Si_xGe_{1-x}, modulation doped field effect transistors and 1.3μm optoelectronics can be identified (Schuppen and Dietrich (1995)).

There are a number of techniques used to grow single crystal Si_xGe_{1-x} alloys. The Czochralski (Cz) crystal growth technique is currently the most efficient method for producing bulk Si_xGe_{1-x} crystals. However, since the liquidus and solidus curves in the Si_xGe_{1-x} phase diagram are widely separated, producing compositionally uniform material requires that silicon be replenished during growth from the melt (Yonenaga (2005)). Similarly in Bridgman growth of Si_xGe_{1-x} alloys, the transport of the species and the changing composition of the melt are again important for producing compositionally uniform crystals (Yesilyurt, Vusijic, Motakel, Szofran, and Voltz(1999); Volz, Schweizer, Kaiser, Cobb, Vujisic, Motakef, and Szofran(2002);

and Volz, Walker, Schweizer, Cobb, and Szofran (2005)).

Liquid Phase Diffusion (LPD) is a solution growth technique used for Si_xGe_{1-x} growth. In LPD, an applied temperature gradient drives silicon diffusion across the germanium melt to initiate growth, and uniform transport across the growth cell is required for homogeneous growth in this technique (Yildiz, Dost, and Lent (2005)).

In the LPD growth setup, the silicon source is placed at the top of the melt, and silicon feed material dissolves into a germanium melt in the opposite direction to the gravity-induced buoyancy force. Due to the large density difference between the silicon solute and the germanium-rich melt, the lighter silicon solute is buoyant in the melt, and diffuses towards the germanium seed in the opposite direction to natural convection. This makes the silicon transport in this system diffusion-dominated and leads to a very stable but slow growth process.

The dissolution process of the source silicon into the germanium melt plays a significant role and is one of the limiting factors for growth rate. We have therefore carried out experimental and numerical studies to shed light into this process with and without the application of magnetic fields (Armour, Dost, and Lent (2007); Armour and Dost (2007, 2009, 2010)).

The effect of an applied magnetic field (static or rotating) on the melt flow depends on the characteristics of the system such as densities of the components of the melt, the electric conductivity of the melt, the level of applied temperature gradients, the geometry, etc. Static fields provide suppression where the convective flows are strong, and rotating fields provide forced mixing changing the flow structures of the melt. Magnetic fields have been utilized in all methods of crystal growth to optimize growth with varying effects (a rich list of references can be found in Series and Hurle (1991); and Dost and Lent (2007)).

Simulations performed using the commercial package Ansys CFX exhibited convergence problems in the presence of magnetic body forces (Armour and Dost(2007)), which could only be resolved by scaling down the body forces significantly due to the unavailability of the source code. Thus in this study, as a continuation of our efforts (Armour, Dost, and Lent (2007); Armour and Dost (2007, 2009, 2010)), we have simulated the dissolution process under an applied static magnetic field using FASTEST and OpenFOAM. Results are compared with experiments.

1.2 The Simulation Problem

As mentioned earlier, the dissolution process observed during crystal growth is important. In this direction we selected the dissolution experiments performed by Armour and Dost (2007) for simulation. The experiments indicate that an applied static magnetic field suppresses convection in the melt but enhances the silicon dis-

solution rate along the source near the crucible walls, as seen from the processed samples in Fig.1.1b. This was not expected since the system was designed to be isothermal. It may imply that the system might have had some unaccounted temperature gradient. We therefore wanted to a have further look into this issue by simulating the process numerically.

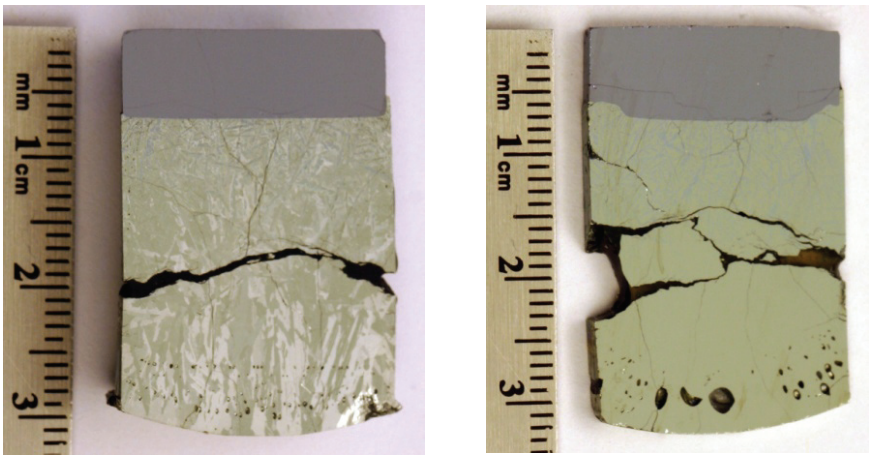

a) no magnetic field b) at a 0.8-tesla static magnetic field

Figure 1.1: Processed samples of dissolution experiments after 20 minutes of dissolution (Armour and Dost(2007). The sections near the crucible wall along the source were dissolved more that the centre section.

Details of the dissolution experiments can be found in Armour and Dost (2007). The crucible, schematically shown in Fig.2.1, was hung in the furnace on a stainless steel rod. It was first preheated for approximately 1 hour above the hot zone at approximately 800˚C. To start the experiment, the crucible was dropped into the isothermal area (at 1100˚C) of the furnace from the preheating position. It was allowed to remain there for the selected experiment time (durations of 10, 20 or 30 minutes). At the conclusion of the experimental time, the crucible was pulled from the furnace and quickly quenched in ice-water. The samples were then sectioned axially into two bulk halves and a 2mm thick center slice. All pieces were polished for analysis (see two samples in Fig.1.1).

2 The Simulation Model

The silicon source, solution (germanium melt), and the side and bottom wall of the quartz ampoule are included in the simulation domain, as shown in Fig.2.2. The

solid domains were not included in the simulations performed with OpenFOAM. Instead, only the melt was considered with a high resolution, and the boundary conditions were adapted accordingly.

Below the field equations of the liquid phase (germanium-rich melt) is introduced. The field equations of the solid phase (quartz wall) consist of only the heat conduction equation, so it is not presented here.

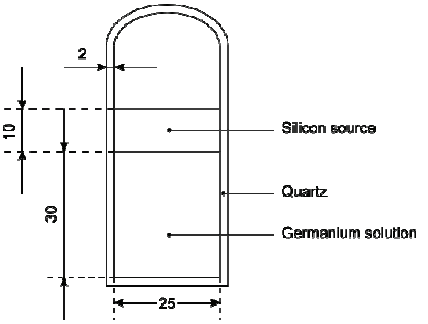

Figure 2.1: Schematic view of the dissolution crucible (dimensions in mm).

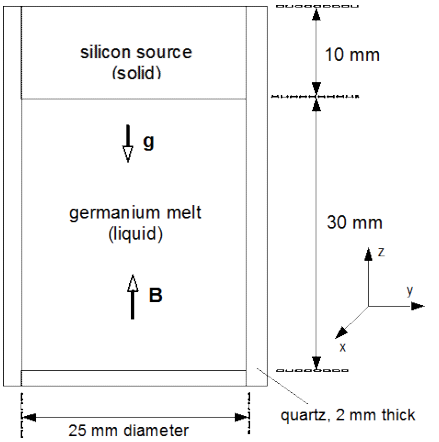

Figure 2.2: Numerical simulation domain.

2.1 Field Equations of the Liquid Phase

The field equations of the liquid phase are the well-known continuity, momentum, energy, and species transport equations written for a Newtonian, incompressible liquid binary mixture subject to a magnetic body force induced by an applied static vertical magnetic field. These equations are written in components form as follows:

Continuity

$$\frac{\partial u_i}{\partial x_i} = 0 \tag{2.1}$$

Momentum

$$\frac{\partial}{\partial t}(\rho u_i) + \frac{\partial}{\partial x_j}(\rho u_i u_j) = \frac{\partial}{\partial x_j}(\mu \frac{\partial u_i}{\partial x_j}) - \frac{\partial P}{\partial x_i} + \rho g_i + F_i \tag{2.2}$$

Energy

$$\frac{\partial}{\partial t}(\rho c_p T) + \frac{\partial}{\partial x_j}(\rho c_p T u_j) = \frac{\partial}{\partial x_j}(\lambda \frac{\partial T}{\partial x_j}) \tag{2.3}$$

Mass transport

$$\frac{\partial}{\partial t}(\rho C) + \frac{\partial}{\partial x_j}(\rho C u_j) = \frac{\partial}{\partial x_j}(\rho D \frac{\partial C}{\partial x_j}) \tag{2.4}$$

2.2 Gravitational Body Force and Boussinesq Approximation

An assumption that significantly simplifies solving the momentum balance equation in Eq.(2.2) is that the mixture (melt) density is taken as constant everywhere except in the body force term on the right hand side. This is known as the Boussinesq approximation and leads to acceptable results when changes in density are small and do not affect the field variables significantly. In this approximation, density is expanded into a Taylor series as a function of a reference temperature and concentration where the second and higher order terms in the expansion are ignored, i.e.

$$\rho(C,T) = \rho_0 + \left.\frac{\partial \rho}{\partial T}\right|_{T_0,C_0}(T-T_0) + \left.\frac{\partial \rho}{\partial C}\right|_{T_0,C_0}(C-C_0) \tag{2.5}$$

where

$$\beta = \frac{\partial \rho}{\partial T}|_{T_0,C_0}, \quad \beta_C = \left.\frac{\partial \rho}{\partial C}\right|_{T_0,C_0} \tag{2.6}$$

are the thermal and solutal expansion coefficients, respectively. Then the gravitational body force is expressed as

$$\rho g_i = \rho_0 g_i + g_i\{\beta_T(T-T_0) + \beta_C(C-C_0)\} \tag{2.7}$$

The constant term $\rho_0 g_i$ can be added to the pressure term in the momentum equation by defining a new pressure as $p = -P + \rho_0 g_z$. Eqs.(2.2) -(2.4) are then written respectively as

$$\rho_0\{\frac{\partial u_i}{\partial t} + \frac{\partial u_i}{\partial x_j}u_j\} = \mu \frac{\partial^2 u_i}{\partial x_i \partial x_j} - \frac{\partial p}{\partial x_i} + g_i\{\beta_T(T-T_0) + \beta_C(C-C_0)\} + F_i \tag{2.8}$$

$$\frac{\partial T}{\partial t} + \frac{\partial T}{\partial x_j}u_j = \frac{\lambda}{\rho_0 c_p}\frac{\partial^2 T}{\partial x_j \partial x_j}, \quad \frac{\partial C}{\partial t} + \frac{\partial C}{\partial x_j}u_j = D\frac{\partial^2 C}{\partial x_j \partial x_j} \tag{2.9}$$

where the condition of incompressibility, i.e., Eq.(2.1), must be satisfied independently.

There are some issues related to the handling of mass concentration appearing in the last term of Eq.(2.7). First, the values of the solutal expansion coefficient available in the literature must be used with care. It makes a big difference whether it is given in mass or molar concentrations. While the solutal expansion coefficient is given in mass or molar percentages, computer codes typically use values between zero and one. The resulting body force differs by a factor of 100 if the conversion is not carried out correctly.

Furthermore, while the thermal expansion coefficient is measured reasonably well at least for elemental silicon and germanium, to the best of our knowledge, no solutal expansion measurements have been done for liquid silicon-germanium solutions. The reliability of the experimental available data is not so good. In order to determine the sensitivity of the system, we have also used a smaller value for the solutal expansion coefficient.

In the dissolution system considered here the solutal buoyancy is the driving force for convection in the melt since the system is isothermal initially (see Armour, Dost and Lent(2007) for details). However, during the dissolution process under applied magnetic field thermal buoyancy may have very small contribution due to small changes in the body forces and thermal field. In the presence of an applied thermal gradient (as is the case of non-isothermal example in this work, or in the growth of SiGe (Armour and Dost(2009, 2010), Yesilyurt, Vusijic, Motakel, Szofran and Voltz(1999)), the contribution of thermal buoyancy may become significant depending on the magnitude of the applied temperature gradient.

FASTEST implements the Boussinesq approximation for temperature variations, but the effect of concentration variations on the mixture density was not taken into account. Thus, the code had to be extended to include solutal buoyancy. As discussed later in detail, this modification was validated using a square cavity test case based on work done by Bergman and Hyun(1996). The same benchmark is used to validate the OpenFOAM implementation.

2.3 Magnetic Body Force Components and the Maxwell Equations

Since the domain is subject to an applied magnetic field, the system equations will naturally include the well-known Maxwell equations in terms of induced electric and applied magnetic fields. Under the well-known magnetohydrodynamic (MHD) approximation and the assumption that the liquid phase is non-magnetizable and nonpolarizable, these equations take the following forms (Chandrasekhar(1961),

Hughes and Young(1966), Dost and Lent(2007)):

$$\nabla \cdot \mathbf{J} = \mathbf{0}, \quad \nabla \cdot \mathbf{B} = \mathbf{0}, \quad \nabla \times \mathbf{E} = -\frac{\partial \mathbf{B}}{\partial t}, \quad \nabla \times \mathbf{B} = \mu_M \mathbf{J} \tag{2.10}$$

and the magnetic body force induced by the applied magnetic field simplifies to

$$\mathbf{F} = \mathbf{J} \times \mathbf{B} \tag{2.11}$$

where the electric current is given by

$$\mathbf{J} = \sigma_E(\mathbf{E} + \mathbf{u} \times \mathbf{B}) \tag{2.12}$$

When the induced electric field is not taken into account, by using Eq.(2.12) in Eq.(2.11) we obtain

$$\mathbf{F} = \sigma_E(\mathbf{u} \times \mathbf{B}) \times \mathbf{B} \tag{2.13}$$

In the following we consider two models which are tested with two benchmark cases of Ben Hadid and Henry(1996, 1997).

2.3.1 Variable Magnetic Field

Using Eq.$(2.10)_4$ in the magnetic body force term given in Eq.(2.11) we write (Chandrasekhar (1961); Kumar, Dost and Durst (2007))

$$\mathbf{F} = \frac{1}{\mu_M}(\nabla \times \mathbf{B}) \times \mathbf{B} = -\frac{1}{\mu_M}\mathbf{B} \times (\nabla \times \mathbf{B}) = \frac{1}{\mu_M}(\mathbf{B} \cdot \nabla)\mathbf{B} - \frac{1}{2\mu_M}\nabla \mathbf{B}^2 \tag{2.14}$$

Using the above form of the magnetic body force, an additional equation is introduced and solved for $\mathbf{B}$. The third Maxwell equation, Eq.$(2.10)_3$, describes the change of the magnetic field with time and is used as a starting point to derive an additional equation. Replacing the induced electric field in Eq.$(2.10)_3$ with Eq.(2.12) leads to the following equation

$$\nabla \times (\frac{\mathbf{J}}{\sigma_E} - \mathbf{u} \times \mathbf{B}) = -\frac{\partial \mathbf{B}}{\partial t} \tag{2.15}$$

The use of Eq.$(2.10)_4$ in the above equation leads to the desired equation for the time varying magnetic field, i.e.

$$\frac{\partial \mathbf{B}}{\partial t} = \nabla \times (\mathbf{u} \times \mathbf{B}) - \nabla \times (\frac{\nabla \times \mathbf{B}}{\mu_M \sigma_E}) \tag{2.16}$$

If the magnetic permeability is assumed constant, and the following identities are used

$$\nabla \times (\nabla \times \mathbf{B}) \equiv \nabla(\nabla \cdot \mathbf{B}) - \nabla^2 \mathbf{B} = -\nabla^2 \mathbf{B} \tag{2.17}$$

and

$$\nabla \times (\mathbf{u} \times \mathbf{B}) \equiv (\mathbf{B} \cdot \nabla)\mathbf{u} - \mathbf{B}(\nabla \cdot \mathbf{u}) + \mathbf{u}(\nabla \cdot \mathbf{B}) - (\mathbf{u} \cdot \nabla)\mathbf{B} = -(\mathbf{B} \cdot \nabla)\mathbf{u} - \mathbf{B}(\mathbf{u} \cdot \nabla) \tag{2.18}$$

we finally arrive at

$$\frac{\partial \mathbf{B}}{\partial t} = \eta \nabla^2 \mathbf{B} - (\mathbf{B} \cdot \nabla)\mathbf{u} - \mathbf{B}(\mathbf{u} \cdot \nabla) \tag{2.19}$$

with $\eta \equiv \frac{1}{\sigma_E \mu_M}$.

The above resulting equation is very similar to the momentum equation and can be solved by similar means. This similarity is most obvious in the magnetic diffusivity η which has the same units as the diffusivity of momentum (kinematic viscosity). To solve this equation, and also ensure the magnetic field stays divergence-free (Eq.$(2.10)_2$, analogous to the continuity equation for incompressible fluids), an artificial magnetic field pressure is introduced. The pressure term will tend to zero for a converged solution and is only needed to solve the equation by the PISO algorithm common for the momentum equation. Additional boundary conditions for the magnetic field and the magnetic field pressure will have to be specified using this approach.

The solution approach outlined in this section is common in MHD flows of plasmas, but requires knowledge of the magnetic permeability material property. A reasonable assumption for conducting liquids is to use the permeability of vacuum (Huges and Young (1966)), however it can be avoided using a different approach to express the magnetic body force. Also, since four additional equations will be solved, this approach requires the most computing power.

2.3.2 Induced Electric Field

Using Eq.(2.12) in Eq.(2.11) we write the magnetic body force as

$$\mathbf{F} = \sigma(\mathbf{E} + \mathbf{u} \times \mathbf{B}) \times \mathbf{B} \tag{2.20}$$

where $\mathbf{E}$ is the induced electric field due to the applied magnetic field, and since it presents an additional variable an additional equation is needed to fully specify the

problem. This equation, given in terms of the electric scalar potential defined by $\mathbf{E} = -\nabla\varphi_E$, is obtained by taking the divergence of Eq.$(2.10)_4$ and using $\nabla \cdot (\nabla \times \mathbf{B}) = 0$ as

$$\nabla^2 \varphi_E = \nabla \cdot (\mathbf{u} \times \mathbf{B}) \tag{2.21}$$

The inclusion of Eq.(2.21) increases the computational cost moderately.

2.4 Boundary and Initial Conditions

Boundary conditions for the flow velocity, temperature, and concentration fields have to be set to fully specify and solve the transport equations. Since concentration and flow velocity are not computed outside the liquid region, conditions only have to be set on the boundaries of the liquid zone.

2.4.1 Flow and Pressure

For the flow velocity, non-slip conditions are used at the crucible walls and the source-solution interface, i.e.

$$u|_{wall} = 0 \tag{2.22}$$

A problem with the pressure solution is that in the closed crucible, all domain boundaries will be assigned a Neumann type, zero-gradient boundary condition:

$$\left.\frac{\partial P}{\partial n}\right|_{wall} = 0 \tag{2.23}$$

Fortunately in such systems the absolute value of the pressure is not of interest and a solution can be obtained by setting a fixed pressure in an arbitrary point.

2.4.2 Concentration

At the crucible walls a no mass-flux condition is applied. This leads to

$$\left.\frac{\partial C}{\partial n}\right|_{wall} = 0 \tag{2.24}$$

At the dissolution interface the saturation condition is applied:

$$C|_{interface} = 1 - \frac{1}{\sqrt{395}}\{\sqrt{1412 + \frac{1600}{395} - T} - \frac{40}{\sqrt{395}}\} \tag{2.25}$$

This condition is derived from the silicon-germanium phase diagram (Levinshtein, Rumyantsev, Shur(2001)) with C denoting the concentration of silicon in molar fraction (simulation results plotted in atomic % to compare with experiments) and T being the temperature in Kelvin.

2.4.3 Thermal field

It is assumed that the heat flux and temperature are continuous across the liquid-solid interfaces,

$$T_{liquid} = T_{solid}, \quad \lambda \left.\frac{\partial T}{\partial n}\right|_{liquid} = \lambda \left.\frac{\partial T}{\partial n}\right|_{solid} \tag{2.26}$$

and Dirichlet type boundary conditions are used at the outer walls of the quartz crucible

$$T|_{cruciblewall} = 1373K \tag{2.27}$$

The initial velocities are set to zero, as well as the initial silicon concentration in the melt. The domain is initialized to 1073 K. For the FASTEST computations, the boundary condition at the crucible walls is set to 1373 K. For the simulations with OpenFOAM the temperature at the lower and side domain boundaries was linearly raised up to 1373 K within 90 seconds.

2.4.4 Induced Electric Field

The quartz ampoule (the border of the computational domain) is an insulator, so the current density normal to the quartz wall will be equal to zero, i.e.

$$\mathbf{J} \cdot \mathbf{n} = 0 \tag{2.28}$$

The use of this condition in Eq. (2.12) leads to a boundary condition for the induced electric field. Knowing that the flow velocity will be zero at a no-slip, non-permeable boundary, the boundary condition reduces to a zero normal gradient of the electric scalar potential:

$$\frac{\partial \varphi}{\partial n} = (\mathbf{u} \times \mathbf{B}) \cdot \mathbf{n} = 0 \tag{2.29}$$

2.4.5 Variable Magnetic Field

On surfaces normal to the magnetic field flux, a Dirichlet condition is set

$$B|_{axial} = B_0 \tag{2.30}$$

On all other surfaces, a Neumann condition is chosen

$$\left.\frac{\partial B}{\partial n}\right|_{sidewall} = 0 \tag{2.31}$$

As for the physical pressure, Neumann conditions for the artificial magnetic pressure are set on all walls. To solve the variable magnetic field equations with these boundary conditions, the magnetic field pressure is set to a constant value at an arbitrary location in the domain.

Table 2.1: Thermophysical properties of the Si-Ge system.

Property	Material	Symbol	Value	Unit	Reference
Density	Solution Source Quartz	ρ	5490 2301 2200	kg/m^3	1
Viscosity	Solution	μ	7.4×10^{-4}	kg/m.s	
Thermal conductivity	Solution Source Quartz	λ	43.0 23.7 2.0	W/m.K	2
Specific heat	Solution Source Quartz	c_p	387 976 1200	J/kg.K	1
Expansion coefficients: thermal solutal	Solution	β_T β_C	0.94×10^{-4} 0.0053	1/K 1/mol%	1 2,3
Electric conductivity	Solution	σ_E	1.405×10^6	1/Ωm	4
Diffusion coefficient	Solution	D	2.5×10^{-8}	m^2/s	5
Prandtl number	Solution	Pa	0.007		

References: 1. Nakamura and Hibiya (1992); 2. Yamasue et al. (2002); 3. Yildiz (2006); 4. Schnygders and Van Zytvelt (1996); 5. Potze (2004).

2.5 Physical Parameters

The physical properties of the silicon source, the germanium solution and the quartz crucible are listed in Table 2.1. The solution is treated as a binary dilute mixture with a small amount of solute (silicon), so the mixture properties will be close to those of liquid germanium. Much material property data have been collected in the 1960's and early 70's, before interest in germanium faded and silicon became the dominant material used in semiconductor technology. Not all of the available data is reliable (Levinshtein, Rumyantsev and Shur(2001)) since measurements are problematic due to difficulties associated with the high melting temperatures of

silicon and germanium. In particular, the solutal expansion and the binary diffusion coefficients are not well measured.

3 Numerical Solution

To investigate the flow and concentration structures in the melt, the governing equations and boundary conditions are discretized and solved numerically. The preprocessors used to mesh the solution domain are Ansys ICEM and the OpenFOAM utility blockMesh. The ICEM grid was used together with FASTEST 3D and the blockMesh grid together with OpenFOAM to solve the equations introduced in the previous chapter.

3.1 Grids and Mesh Quality

The quality of a structured grid, which is measured in quantities like control volume angles and control volume edge ratio, has a large impact on the convergence of a simulation because the finite volume method is sensitive to grid distortions. Grid distortions appear when mapping the hexagonal elements to round shapes, e.g. when meshing a pipe. A good way to create the blocking is to employ an O-Grid using five blocks: a cuboid block in the centre of the round domain and four trapezoidal blocks around the centre cuboid. The trapezoidal blocks produce much favourable elements when mapped to the round geometry.

FASTEST 3D works with block-structured (multiblock) meshes that can be generated by Ansys ICEM, a commercial grid generator. OpenFOAM includes mesh conversion utilities for meshes in various formats, however the included blockMesh utility works well for primitive shapes and was found more convenient to use. blockMesh is a command-line tool that uses an input file defining key geometric locations, connections between those points and blocking information to generate a mesh.

In the cylindrical magnetic force benchmark, OpenFOAM turned out to be less sensitive to grid distortions than FASTEST. Grid optimization is a bit easier using ICEM due to the immediate visual feedback it provides, however, OpenFOAM is more tolerant towards grid quality so less optimization was needed and the use of blockMesh was sufficient. FASTEST and OpenFOAM provide two different ways to work with non-optimal grids: FASTEST applies underrelaxation to the equations if convergence is an issue, while OpenFOAM can apply non-orthogonal correctors and automatic time step adjustion. It was found that underrelaxation comes with a greater performance penalty than the non-orthogonal correctors.

The grid used with FASTEST including the source and quartz domains is shown in Fig.3.1. For the simulations done with OpenFOAM the quartz and source domains

were not considered and the boundary conditions have to be adapted accordingly. Since multiple species are only present within the melt, dropping the solid domains only affects the solution of the temperature and induced electric field. The new temperature boundary conditions are based on calculations done with FASTEST and the CFX results of Armour and Dost(2007). Since the particles are stationary in the source material, no electric field is induced by the magnetic field and the boundary conditions used are still the Neumann condition shown in Section 2.4.4.

The grid utilized for the OpenFOAM simulations is displayed in Fig.3.2. With 220 000 control volumes it is finer than the FASTEST grid. To increase the resolution of the Hartmann layer, the grid spacing was refined towards the top and bottom surfaces.

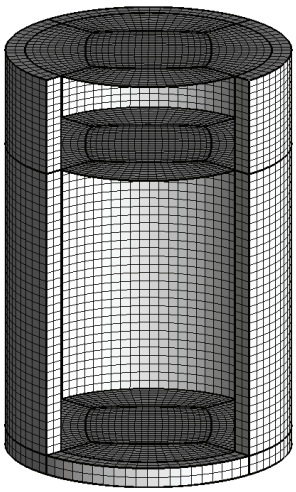

Figure 3.1: Final grid shape (FASTEST).

3.2 Stability Considerations

Using the following identity

$$(\mathbf{u}\times\mathbf{B})\times\mathbf{B} = (\mathbf{B}\cdot\mathbf{u})\mathbf{B} - B^2\mathbf{u} \tag{3.1}$$

the magnetic body force in Eq.(2.20) can be written as

$$\begin{pmatrix} F_x \\ F_y \\ F_z \end{pmatrix} = \sigma_E \begin{pmatrix} A_x + wB_xB_z - uB_z^2 - uB_y^2 + vB_xB_y \\ A_y + uB_yB_z - vB_x^2 - vB_z^2 + wB_yB_z \\ A_z + vB_zB_y - wB_y^2 - wB_x^2 + uB_zB_x \end{pmatrix} \tag{3.2}$$

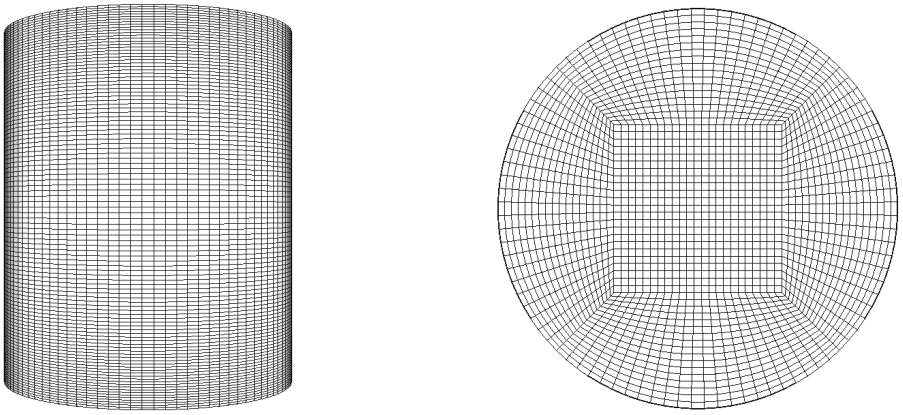

Figure 3.2: High resolution grid used for OpenFOAM simulations: a) side view, and b) top view.

where A_x, A_y, and A_z denote additional terms that arise when considering the induced electric field, but are not important for the stability analysis.

The magnetic body force acts on the liquid points, and hence is included in the momentum balance equation on the right hand side. The quadratic coefficients linked to the solution variable will always be negative and cause convergence problems if kept in the source term. To improve convergence, Kumar, Dost, Durst(2007) suggested an implicit treatment by moving the quadratic expressions to the left hand side of the discretized momentum equations, which increases diagonal dominance of the coefficient matrix.

3.3 Validation

The developed source modifications were validated using two benchmark problems before performing the dissolution simulations.

3.3.1 Solutal Buoyancy Implementation

The source code modification to support solutal buoyancy was validated using a test case presented by Bergman and Hyun(1996). Bergman and Hyun conducted two dimensional simulations of the flow velocity, temperature, and concentration fields of liquid Pb-Sn exposed to horizontal gradients of temperature and species. From the range of parameters investigated by them, the results for a simulation on a grid of 65×65 nodes, a Rayleigh number of Ra=100 and a buoyancy ratio N =

-10 were selected for comparison.

Concentration contours as well as streamlines were computed at non-dimensional times 0.75, 1.35 and 3.15. The results obtained are in agreement with the values found in the reference article of Bergman and Hyun(1996) (see Kidess(2009) for details).

3.3.2 Magnetic Field Implementation

Three different implementations for the magnetic field described in detail in section 2.4 have been validated using two studies by Hadid and Henry(1996, 1997) as reference. In the following, the setup found in reference Hadid and Henry(1996) will be referred to as the cavity benchmark and reference Hadid and Henry(1997) as the cylinder benchmark.

The cavity benchmark was evaluated at $Ha = 100$ and $Gr = 10^4$. The cylinder benchmark parameters were $Ha = 150$ and $Gr = 5\times10^4$. The configuration of the magnetic field aligned with gravity turned out to be the most problematic in terms of the reproducibility of the results accurately. Thus the results presented in the following sections are based on that configuration.

3.3.3 Cavity Benchmark

Compared to the reference article, a slightly higher grid resolution of 35x19x19 was used.

Without any additional equation, transversal flow is inhibited everywhere except at the very ends of the pipe. The longitudinal flow is constant over the width of the channel and varies linearly over its height. This only very roughly matches the benchmark results.

Better results were obtained using an additional equation to describe a variable magnetic field, but also did not show flow patterns that fully satisfy the reference article results. The global flow pattern is similar, but the curvature of the velocity profile (x and z components) is far less pronounced.

Including the induced electric field into the simulations as in the reference article leads to the results that satisfy the benchmark.

3.3.4 Cylinder benchmark

The grid resolution used is $27\times27\times82$ for the centre block and $35\times27\times82$ for the outer O-Grid blocks. This is significantly higher than the number of nodes used in the reference paper and was needed to smooth out errors at the block boundaries. The spectral element method used in the reference paper seems to perform better

on distorted elements. FASTEST had more problems with block boundary artifacts than OpenFOAM.

Without any additional equation, transversal flow is inhibited everywhere except at the very ends of the pipe. Some artifacts are visible at the O-Grid block borders. Again, benchmark results using the variable magnetic field approach were better than using no additional equations to determine the magnetic force, but the flow patterns obtained don't quite satisfy the reference paper results. However, the maximum velocity values and are in good agreement. Out of the three magnetic field implementations, using a variable magnetic field is the most computationally expensive. The inclusion of induced electric field into the simulations as in the reference article leads to the results that satisfy the benchmark.

4 Simulation Results of the Dissolution Process, and Discussion

Simulations with FASTEST including the silicon source and the quartz crucible on three sides confirmed that the isothermal state is reached after about 90 seconds. The computed temperature agrees well with the CFX results obtained by Armour and Dost(2007). Both results may actually slightly underestimate the transient temperature, because they only include conduction in the solid bodies. At high temperatures radiation can be the dominant heat transfer mechanism through the quartz wall (Potze(2004)) and the isothermal state would be reached even earlier. Based on these results a 90 second linear ramp was used as boundary condition for the simplified simulations using OpenFOAM.

The Crank-Nicholson time marching scheme performed well in the benchmarks (see previous chapter), but turned out to be unstable for the silicon dissolution simulations without magnetic fields. The simulations converged with the PISO coupling scheme and very small time steps, but showed numerically driven oscillations in the concentration isolines. Using the implicit Euler time marching scheme both PISO and transient SIMPLE algorithms would converge and give the expected results presented in the following sections.

4.1 Dissolution under Isothermal Conditions

The dissolution experiments performed by Armour and Dost(2007) are designed to be under isothermal conditions. In this section we present the simulation results obtained with OpenFOAM under the assumption of isothermal boundary conditions to simulate the dissolution process of silicon into germanium melt.

The simulations were carried out with and without the application of magnetic field. Fig. 4.1 shows concentration contour plots in a $y-z$ plane cut for simulations with and without magnetic field. The difference in concentration values in Fig.4.1a and

Fig.4.1b is very small, not notable in the scale that the figures are plotted. The application of a magnetic field of 0.8 tesla however causes a slight curvature in the concentration isolines near the dissolution interface (notable at the upper region of Fig.4.1.b) due to the altered flow structure (as seen in Fig.4.2b), as indicated by experiments (Fig.1.1). In both cases the concentration evolution is diffusion dominated, leading to a homogeneous radial concentration field.

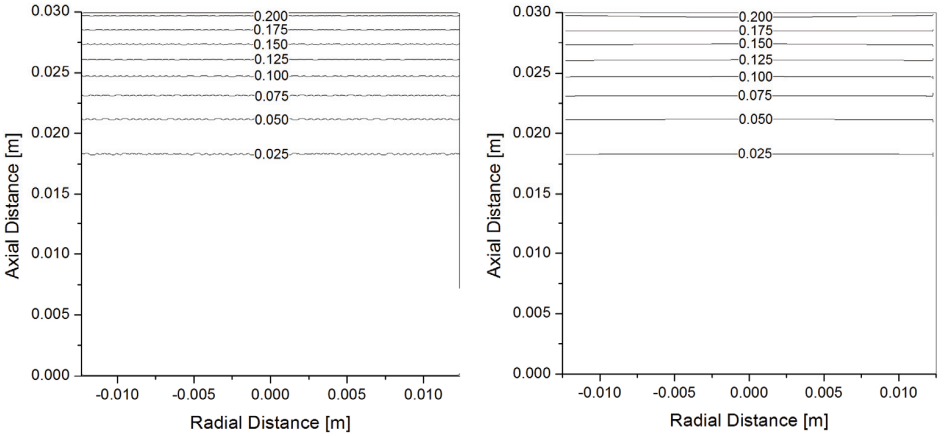

a) no magnetic field b) at 0.8 tesla magnetic field

Figure 4.1: Concentration isolines after 20 minutes of dissolution (in % / 100).

The computed flow structures are shown in Fig.4.2, and the altered flow field under magnetic field is more pronounced than the concentration field. As seen in Fig.4.2b, the application magnetic field changes the flow velocity directions more than the flow intensity. Changes in the flow field are due to the contributions of the magnetic body force components in the momentum equations. Thin Hartmann layers are visible at the upper and bottom of the regions (Fig. 4.2b), which show velocity vectors in the *y*-*z* plane at 1200 seconds of dissolution. As seen from the figure, there is no visible flow outside the Hartmann layer.

Fig.4.3 shows the silicon concentration values along the height of the liquid zone at the centerline and along a parallel line offset by 1 cm from the liquid zone centre. For the case with no magnetic field, the concentration gradient at the interface is identical at the centerline and the offset location, whereas under magnetic field, the gradient at the centerline is less steep. Dissolution is proportional to the concentration gradient and more dissolution would be expected where the gradient is steeper. The numerical results here do show the trend of higher axial concentration gradients away from the center of the melt. Therefore, more dissolution would be

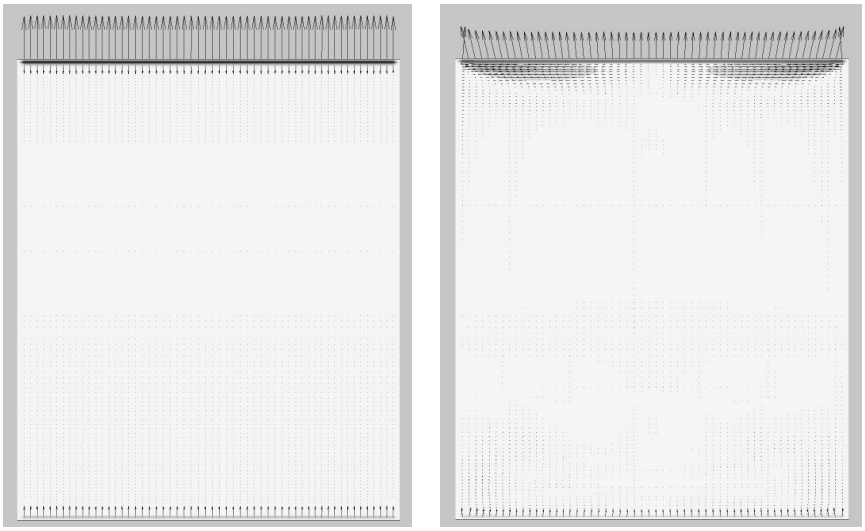

a) no magnetic field b) at 0.8 tesla magnetic field

Figure 4.2: Velocity vectors in a plane cut normal to the x-direction in the melt. Arrows at the upper and lower boundaries of the computational domain represent the flow velocity vectors along the dissolution interface and the bottom of the germanium melt.

expected near the wall. However, the numerical results do not predict the significant enhancement that was seen in experiment. The effect in this numerical work is quite small.

Fig.4.4 presents the concentration measurements from the samples in Fig.1.1, which are in general agreement (in behaviour and values) with the simulations results. However, the experimentally observed enhanced dissolution structure near the ampoule wall is not described fully by this model. The correct trend to more dissolution near the wall would be driven by the steeper concentration gradient away from the center. However, the magnitude of this effect in the simulation model is insufficient to explain the enhanced dissolution at the crucible wall observed in experiment.

4.2 Dissolution under a Temperature Gradient

As seen from the simulation results presented in the previous section, under the assumption of isothermal conditions the application of a static magnetic field leads to only slightly altered concentration gradients and flow structures in the melt.

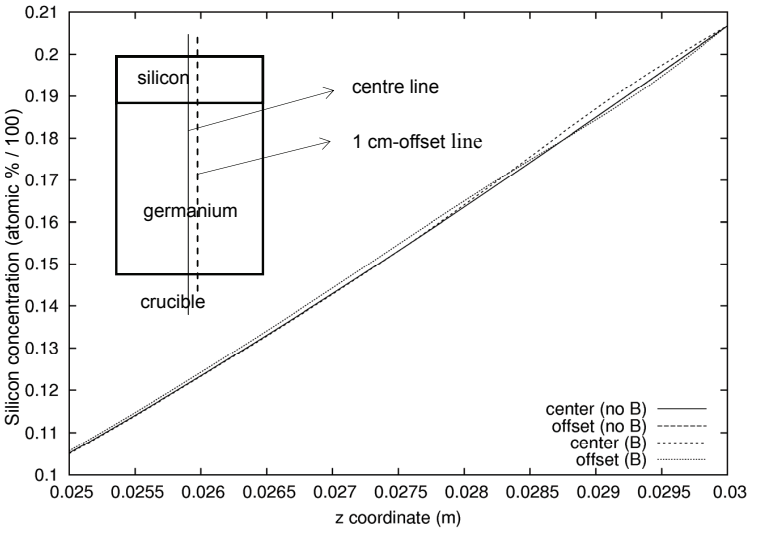

Figure 4.3: Silicon concentration in the upper region of the melt at the center-line and 1-cm offset, with and without magnetic field. The distance measurement is from the bottom of the domain in the vertical direction.

Although the computed concentration distribution in the melt are in agreement with experiments, they do however not predict the experimentally observed enhanced dissolution structure near the wall along the source/melt interface (shown in Fig.1.1b). It may be possible that the presence of such a dissolution structure may be the result of an interaction between a possible unaccounted thermal gradient in the melt and the applied magnetic field.

In order to shed light on this issue, an artificial heat leak that would lead to axial and radial temperature gradients was considered by introducing a temperature gradient into the simulation model. This was realized by applying a fixed heat flux of 420 Watts at the top of the computational domain, corresponding to about 30K temperature reduction at top of the ampoule with respect to the dissolution temperature. A well-designed experimental setup is close to being isothermal. The value of 30K temperature difference is very large and may not be possible unless there are design errors in the experimental setup. We selected such a large value only because we wanted to exaggerate the interaction of the thermal field with magnetic field.

Since the melt is a metallic liquid (with a small Prandtl number of 0.007), it reaches a thermal steady state very quickly. Thus, in the simulations the temperature field is decoupled from the flow field. The computed temperature profile under an applied temperature gradient is shown in Fig. 4.5.

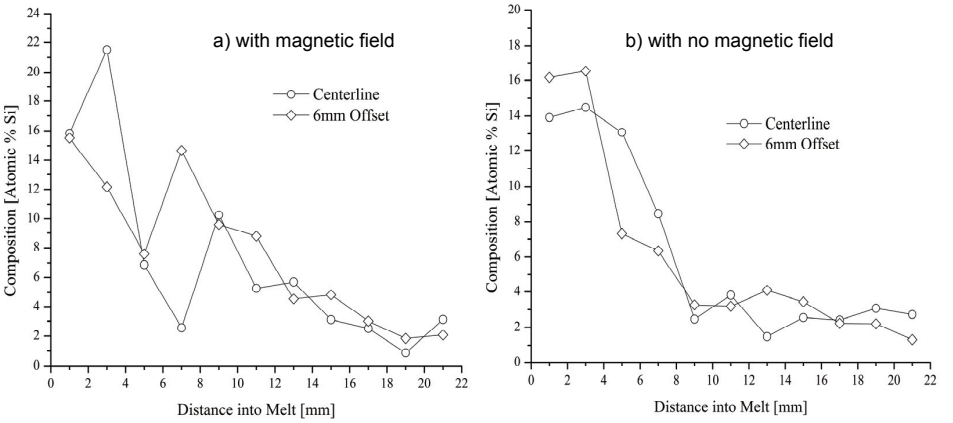

Figure 4.4: The left plot (a) is of the measured silicon concentration (by EDS) from the sample processed under magnetic field (after Armour and Dost(2007). The right plot (b) is measured concentration profile of the sample processed without the applied field. There is a higher concentration of silicon deeper into the melt in the plot on the left, the sample processed with the magnetic field, as predicted by simulations (Fig.4.1b). The measurements are from the source material. The fluctuations in the measured concentration profiles are due to segregation during the quenching process.

The computed concentration contours and velocity field under heat leak are presented in Figs 4.6 and 4.7, respectively. As seen, the difference between the concentration gradients computed with and without magnetic field is less pronounced compared with those of the isothermal case. Also, the steeper concentration gradient near the wall of the crucible is present with and without the application of the magnetic field. This is not supported in the experimental work.

The computed flow velocity fields in Fig.4.7 show that although the flow field was affected under magnetic field, the computed flow structure is similar to that of the isothermal case, with however slightly weaker flow in the germanium melt due to less solutal buoyancy since the upper part of the domain is cooler than the isothermal case. Considering the artificially high value of the applied temperature gradient (which will be very small in a well designed experimental setups) used in the simulation, one can say that the experimental system was actually close to being isothermal.

The effects of applied magnetic field and heat leak on silicon concentration are not so notable on the scale presented in Figs. 4.1 and 4.6, particularly near the dissolution interface where the effects are pronounced in experimental measurements.

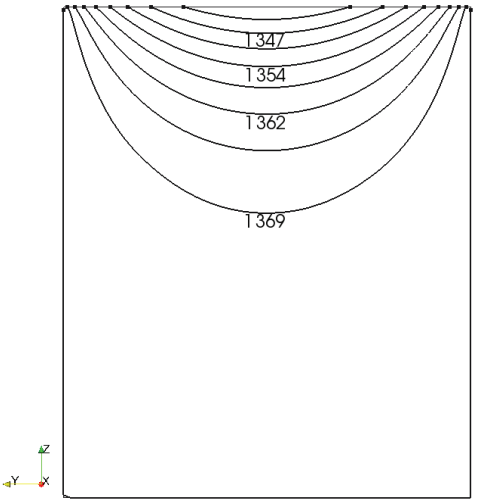

Figure 4.5: Computed temperature distribution under the applied heat leak (in K).

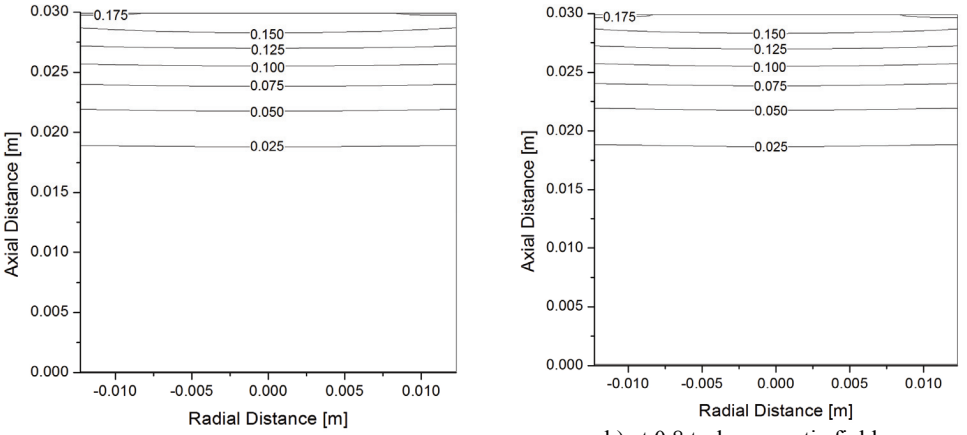

a) no magnetic field

b) at 0.8 tesla magnetic field

Figure 4.6: Concentration isolines with heat leak. Steeper gradients around the edge of the crucible are evident. However, they appear in both the simulations computed with magnetic field and those without.

In order to make them more visible, the silicon concentrations computed along a cross section 2 mm below the interface are presented in Fig. 4.8 using a larger scale. As seen from the figure, the difference in concentration values in the cases of isothermal and heat leak are very visible. The effect of applied magnetic field is

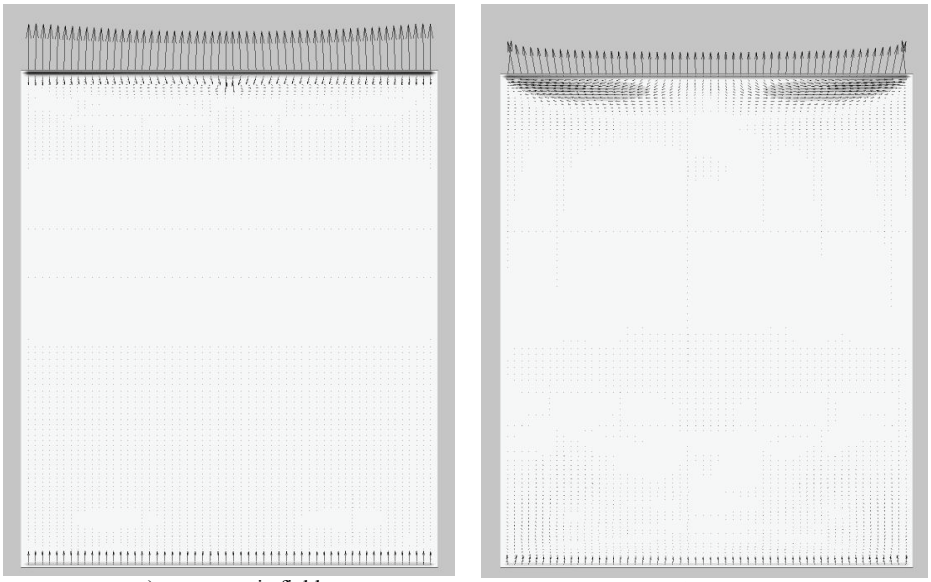

a) no magnetic field b) at 0.8 tesla magnetic field

Figure 4.7: Velocity vectors with temperature gradient. Thin areas of flow are evident around the dissolution interface.

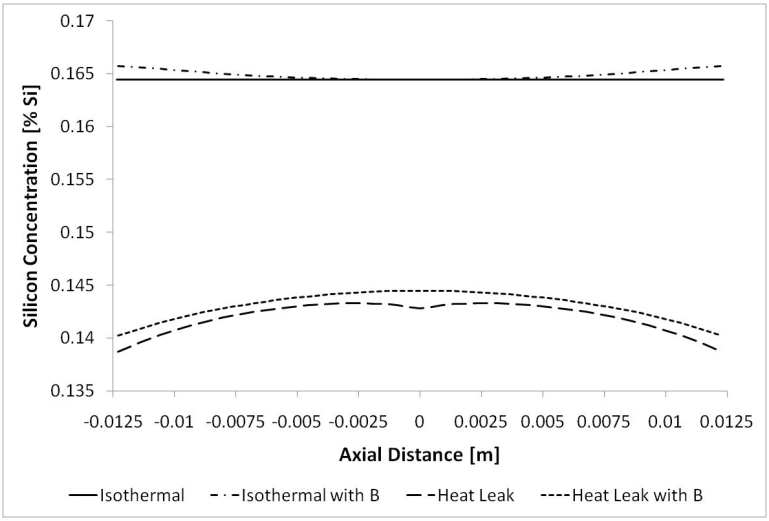

Figure 4.8: Computed radial concentration values along a cross section 2 mm below the dissolution interface.

more pronounced. The radial concentration gradients are also notable in this figure.

As seen, even under the considered heat leak the computed concentration distribution does not predict the experimentally observed enhanced dissolution structure near the ampoule wall along the dissolution interface (see Fig.1.1b). This result may require a closer look on some other parameters such as the contribution of thermoelectromagnetic convection in the present Si-Ge system by including the thermoelectric powers of the solid and liquid phases in the numerical model. As shown by Yesilyurt, Vusijic, Motakel, Szofran and Voltz(1999), thermoelectric currents promote convection in the melt and change the shape of the interface and the concentration field significantly. One may need to develop a full numerical model including thermomagnetoelectric convection for the dissolution example used here in a future work. The reliability of the available physical parameters of the SiGe system used in the simulations may also be reexamined.

5 Conclusion

Two open source codes were utilized and the issues related to handling magnetic body force terms in simulating liquid systems were discussed. The dissolution process of silicon into the germanium melt was selected as an application. The numerical simulations results agree with the experimental silicon concentration distribution in the melt without and with the application of a static magnetic field. The simulation results do not however predict the experimentally observed enhanced dissolution structure near the source under magnetic field. This may require the inclusion of some other parameters such as the effect of thermoelectric powers of the solid and liquid phases in the numerical simulation model. One may also reexamine the reliability of the available physical parameters of the SiGe system used.

Acknowledgement: The financial support provided by the Space Science Enhancement Program (SSEP) of the Canadian Space Agency (CSA), the Natural and Engineering Science Council of Canada (NSERC), and Canada Research Chairs (CRC) Program is gratefully acknowledged.

References

Armour, N.; Dost, S. (2007): The effect of a static magnetic field on buoyancy-aided silicon dissolution into Germanium Melt. *J. Crystal Growth*, vol. 306(1), pp. 200-207.

Armour, N.; Dost, S. (2009): Effect of an applied static magnetic field on silicon dissolution into a germanium melt. *J. Crystal Growth*, vol. 311, pp. 780–782.

Armour, N.; Dost, S.; Lent, B. (2007): Effect of free surface and gravity on

dissolution in germanium Melt. *J. Crystal Growth*, vol. 299, pp. 227-233.

Armour, N.; Dost, S. (2010): Effect of a static magnetic field on silicon transport in liquid phase diffusion growth of SiGe. *Cryst. Res. Technol.*, vol. 45, pp.244-248.

Ben Hadid, H.; Henry, D. (1997): Numerical study of convection in the horizontal Bridgman configuration under the action of a constant magnetic field. Part 2. three-dimensional flow. *J. Fluid Mechanics*, vol. 333, pp. 57–83.

Ben Hadid. H.; Henry, D. (1996): Numerical simulation of convective three-dimensional flows in a horizontal cylinder under the action of a constant magnetic field. *J. Crystal Growth*, vol. 166(1-4), pp. 436–445.

Bergman, T.L.; Hyun, M. T. (1996): Simulation of two-dimensional thermosolutal convection in liquid metals induced by horizontal temperature and species gradients. *Int. J. Heat and Mass Transfer*, vol. 39(14), pp. 2883–2894.

Chandrasekhar, S. (1961): Hydrodynamic and hydromagnetic stability. Clarendon Press, Oxford.

Dost, S.; Lent, B. (2007): *Single Crystal Growth of Semiconductors from Metallic Solutions*, Elsevier, Amsterdam, Netherlands.

Hughes, W.F.; Young, F. J. (1966): The electromagnetodynamics of fluids. Wiley, New York.

Jana, S.; Dost, S.; Kumar, V.; Durst, F. 2006: A numerical simulation study for the Czochralski growth process of *Si* under magnetic field, *Int. J. Engng. Sci.*, 44, 554-573.

Kasper, E. (1995): Prospects of SiGe heterodevices. *J. Crystal Growth*, vol. 150, pp. 921-925.

Kidess, A. (2009): Influence of static magnetic fields and solutal buoyancy on silicon dissolution into germanium melt, MASc Thesis, University of Victoria, Victoria, BC Canada.

Kumar, V.; Dost, S.; Durst, F. (2007): Numerical modeling of crystal growth under strong magnetic fields: An application to the travelling heater method. *Appl. Mathematical Modelling*, vol. 31(3), pp. 589–605.

Levinshtein, M.E.; Rumyantsev, S.L.; Shur, M. (2001): Properties of advanced semiconductor materials: GaN, AIN, InN, BN, SiC, SiGe. Wiley-Interscience.

Nakamura, S.; Hibiya, T. (1992): Thermophysical properties data on molten semiconductors. *Int. J. Thermophysics*, vol.13(6), pp.1061–1084.

Potze, W. (2004): Radiation heat transfer in axisymmetric quartz glass tubes. *J. Quantitative Spectroscopy and Radiative Transfer*, vol. 84(4), pp. 575–586.

Rouzaud, A.; Camel, D.; Favier, J.J. (1985): A comparative study of thermal and

thermosolutal convective effects in vertical bridgman crystal growth. *J. Crystal Growth*, vol.73(1), pp.149–166.

Schnyders, H.S.; Van Zytveld, J.B. (1996): Electrical resistivity and thermopower of liquid Ge and Si. *J. Physics Condensed Matter*, vol.8, pp. 10875–10883.

Schuppen, A.; Dietrich, H. (1995): High speed SiGe heterobipolar transistors. *J. Crystal Growth*, vol. 157, pp. 207-214.

Seidenberg, P. (1997): From germanium to silicon: A history of change in the technology of semiconductors. Facets: New perspectives on the history of semiconductors, in "Facets: New Perspective on the History of Semiconductors" (Eds. A. Goldstein and W. Aspray), IEEE, pp. 36–74.

Series, R.W.; Hurle, D.T.J. (1991): The use of magnetic fields in semiconductor crystal growth. *J. Crystal Growth*, vol.113(1-2), pp. 305–328.

Usami, N.; Kitamura, M.; Obara, K.; Nose, Y.; Shishido, T.; Nakajima, K. (2005): Floating zone growth of Si-rich SiGe bulk crystal using pre-synthesized SiGe feed rod with uniform composition. *J. Crystal Growth*, vol. 284, pp. 57-64.

Volz, M.P.; Schweizer, M.; Kaiser, N.; Cobb, S.D.; Vujisic, L.; Motakef, S.; Szofran, F.G. (2002): Bridgman growth of detached GeSi crystals. *J. Crystal Growth*, vol. 237, pp. 1844-1848.

Volz, M.P.; Walker, J.S.; Schweizer, M.; Cobb, S.D.; Szofran, F.R. (2005): Bridgman growth of germanium crystals in a rotating magnetic field. *J. Crystal Growth*, vol. 282, pp. 305-312.

Yamasue, E.; Susa, M.; Fukuyama, H.; Nagata, K. (2002): Thermal conductivities of silicon and germanium in solid and liquid states measured by non-stationary hot wire method with silica coated probe. *J. Crystal Growth*, vol.234(1), pp.121–131.

Yesilyurt, S.; Vujisic, L.; Motokel, S.; Szofran, F.R. (1999): A numerical investigation of the effect of thermoelectromagnetic convection (TEMC) on the Bridgman growth of $Si_{1-x}Si_x$. *J. Crystal Growth*, vol. 207, pp. 278-291.

Yildiz, E.; Dost, S. (2007): The combined effect of rotating and static magnetic fields in liquid phase diffusion growth of SiGe. *J. Crystal Growth*, vol. 303, pp. 279-283.

Yildiz, E.; Dost, S.; Yildiz, M. (2006): A numerical simulation study for the effect of magnetic fields in liquid phase diffusion growth of *SiGe* Single Crystals. *J. Crystal Growth*, vol. 291, pp. 497-511.

Yildiz, M. (2006): A combined experimental and modeling study for the growth of SixGe1-x single crystals by liquid phase diffusion (LPD), PhD thesis, University of Victoria, Victoria, BC Canada.

Yildiz, M.: Dost, S. (2005): A computational model for the liquid phase diffusion growth of SiGe single crystals. *Int. J. Engng. Sci.*, vol. 43, pp. 1059-1080.

Yildiz, M.; Dost, S.; Lent, B. (2005): Growth of bulk SiGe single crystals by liquid phase diffusion. *J. Crystal Growth*, vol. 280, pp. 151-160.

Yonenaga, I. (2005): Growth and fundamental properties of SiGe bulk crystals. *J. Crystal Growth*, vol. 275, pp. 91-98.